iScience

CellPress
OPEN ACCESS

Article

Active control of electro-visco-fingering in Hele-Shaw cells using Maxwell stress

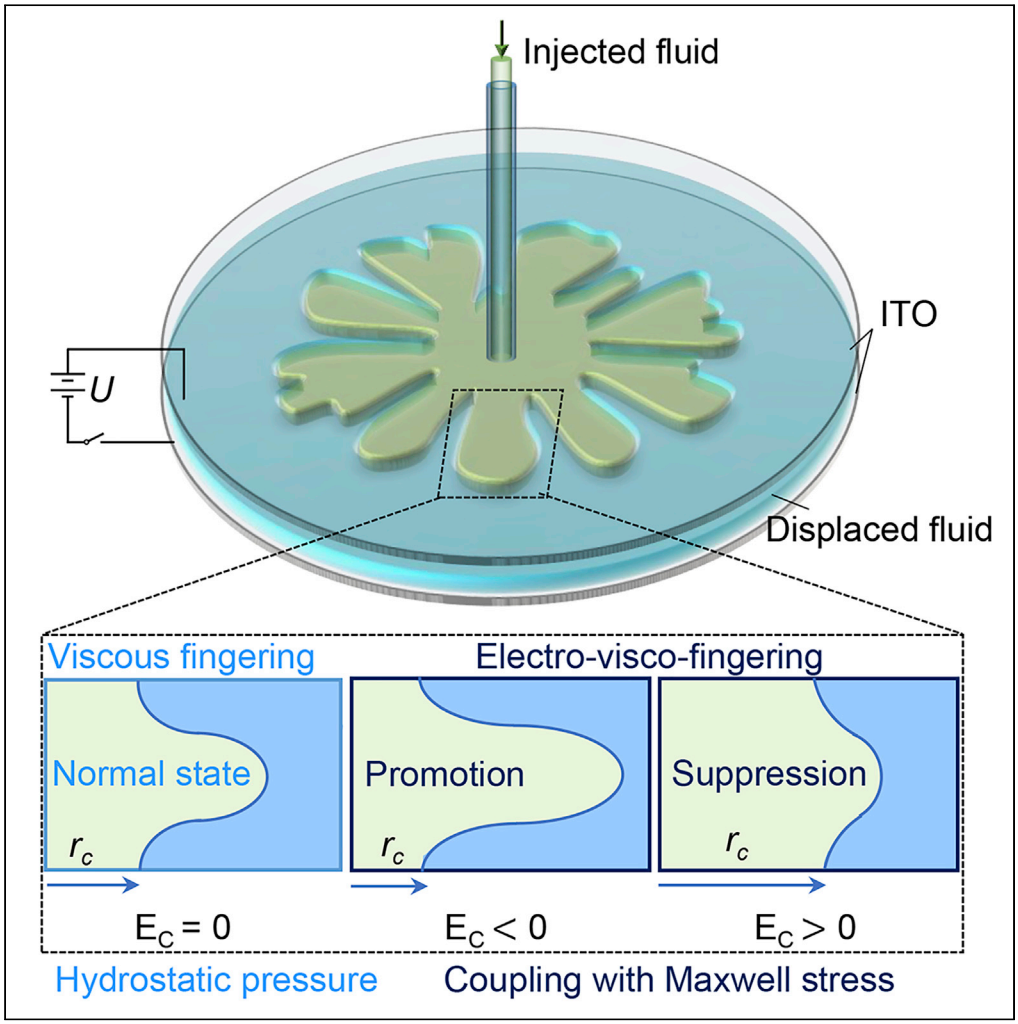

Peiliu Li, Xianfu Huang, Ya-Pu Zhao

yzhao@imech.ac.cn

Highlights

A new type of viscous fingering is actively controlled by applying an electric field

The interfacial instability is controlled by taking advantage of the Maxwell stress

An Electric Control number is adopted to characterize the effect of Maxwell stress

This work provides a new way to actively control viscous fingering for applications

Li et al., iScience 25, 105204
October 21, 2022
https://doi.org/10.1016/j.isci.2022.105204

iScience

CellPress
OPEN ACCESS

Article

Active control of electro-visco-fingering in Hele-Shaw cells using Maxwell stress

Peiliu Li,[1,2] Xianfu Huang,[1,2] and Ya-Pu Zhao[1,2,3,*]

SUMMARY

Viscous fingering is an extensively observed phenomenon in porous media or Hele-Shaw cells. In general, this instability is particularly difficult to control for given fluids and geometries. Therefore, investigating a control method of viscous fingering is quite attractive. Here, we present that electro-visco-fingering (EVF) in fluids with different relative permittivity shows a controllable performance under electric fields. The theoretical model is established from the perspective of force analysis to indicate that active control of EVF is achieved by the competition between the Maxwell stress jump and hydrostatic pressure gradient. In addition, an Electric Control number (E_C) is adopted to characterize the electric effect on EVF and experimentally confirmed for broad ranges of flow rates and voltages. Unlike the electro-osmotic flow, this method shows a considerable achievement in energy efficiency. Our work provides a new way to actively control viscous fingering and opens new routes for applications of interfacial instabilities.

INTRODUCTION

The displacement of one fluid by another is one of the most common processes involving interfacial instabilities. In porous media or Hele-Shaw cells, the interface of two fluids is universally accepted to be unstable when a less viscous phase invades a more viscous phase: the classical viscous fingering instability (De Wit, 2016; Wooding and Morelseytoux, 1976; Saffman and Taylor, 1958; Homsy, 1987). Some similar unstable interfaces are also discovered in other situations, such as salt fingers in density-driven situations (Alqatari et al., 2020; Bischofberger et al., 2014), "dendritic" patterns in solidification (Benjacob et al., 1985; Brady and Ball, 1984), and the printer's instability of oil confined in journal bearings and between printing rollers (Taylor, 1963; Rabaud et al., 1990). In most cases, interfacial instabilities hinder the operation of processes and limit their efficiency. For example, the "finger-like" pattern reduces the efficiency of oil recovery by water flooding (Gorell and Homsy, 1983; Farajzadeh et al., 2020), and "dendritic growth" is a major defect in crystals and solidification (Jeong et al., 2001; Xu et al., 2014). However, there are situations where interfacial instabilities may be beneficial, such as enhancing CO_2 mixing in saline aquifers for carbon sequestration (Gilmore et al., 2020; Chen et al., 2018; Taheri et al., 2018), improving the mixing efficiency in small-scale devices, or patterning soft materials (Jha et al., 2011; Marthelot et al., 2018). Depending on the application, either the suppression or the promotion of interfacial instabilities is desirable. Therefore, investigating active control of interfacial instabilities, including intentional suppression or promotion, is quite attractive.

Viscous fingering is a classical interfacial instability, and its performance is notably challenging to control. In the early twentieth century, petroleum and mining engineers noticed that water does not displace oil uniformly and that finger-like patterns always occur at the interface when water penetrates oil (Hill, 1952). Owing to the shape of its pattern, this phenomenon is now known as the fingering problem. In the early 1950s, this problem was first studied by Hill (1952) and soon after by Saffman and Taylor (1958) and Chuoke et al. (1959). In particular, a viscous fingering experiment was first conducted by Saffman and Taylor in a Hele-Shaw cell, which was confined between two parallel plates with a narrow space. In the work (Saffman and Taylor, 1958), they found that interfacial instabilities always occur when a low-viscosity phase displaces a high-viscosity phase and performed a linear stability analysis to show that the onset of instability may be controlled only by the viscosity ratio. Therefore, the control of viscous fingering is limited for certain fluids and geometries.

Owing to the fact that the control of viscous fingering is very important in applications, such as enhanced oil recovery (Gorell and Homsy, 1983; Orr and Taber, 1984) and carbon sequestration (Farajzadeh

[1]State Key Laboratory of Nonlinear Mechanics, Institute of Mechanics, Chinese Academy of Sciences, Beijing 100190, China

[2]School of Engineering Science, University of Chinese Academy of Sciences, Beijing 100190, China

[3]Lead contact

*Correspondence: yzhao@imech.ac.cn

https://doi.org/10.1016/j.isci.2022.105204

et al., 2020), fingering instabilities in porous media flows have since been widely studied (Li et al., 2009; Al-Housseiny and Stone, 2013; Peng and Lister, 2020). In recent years, several strategies have been pursued to manipulate the conditions to control viscous fingering, including passive and active methods. Examples of passive control methods include manipulating the Hele-Shaw cell geometry (Al-Housseiny and Stone, 2013; Bongrand and Tsai, 2018; Anjos et al., 2018; Morrow et al., 2019; Dias and Miranda, 2013a, 2013b), using elasto-visco-plastic materials (Eslami and Taghavi, 2017) and elastic-walled cells (Pihler-Puzovic et al., 2012, 2018; Al-Housseiny et al., 2013), employing large gap widths in Hele-Shaw cells (Honda et al., 2006; Kollner et al., 2015; Maes et al., 2010; Islam and Gandhi, 2016), and modifying the wettability (Trojer et al., 2015; Holtzman and Segre, 2015; Anjos et al., 2021). Active manipulation methods are achieved by adjusting the flow rate (Li et al., 2009; Coutinho and Miranda, 2020; Dias et al., 2012; Arun et al., 2020), or gap thickness (Zheng et al., 2015; Vaquero-Stainer et al., 2019) over time, or multiport lifted Hele-Shaw cells (Kanhurkar et al., 2019) and harnessing electro-osmotic flows generated through applying electric fields (Gao et al., 2019; Mirzadeh and Bazant, 2017; Anjos et al., 2022). Although both types of methods can achieve interfacial control, active methods are preferable in applications due to their simple operation. In particular, for the electro-osmotic flow method, researchers (Gao et al., 2019; Mirzadeh and Bazant, 2017) demonstrated that depending on the magnitude and direction of the electric current, viscous fingering instability can be either enhanced or suppressed. The complex viscous fingering is actively controlled by altering an electric field, which is a significant achievement. Nevertheless, viscous fingering is challenging to stay in a closed loop in practical applications, which is the necessary condition of the electro-osmotic flow method. Compared with the electro-osmotic flow method, the Maxwell stress is always formed with an easy operation. Previous studies (Liu et al., 2018; Yuan and Zhao, 2009, 2010; Feng et al., 2009; Tadmor et al., 2002) have revealed that the wettability of a liquid, including the surface tension, contact angle, and movement of the contact line, can be adjusted by an electric field. The solid-liquid, liquid-liquid, and liquid-gas interfacial tension can be altered by the induced residual charge (Schnitzer and Yariv, 2015; Schnitzer et al., 2014; Bazant, 2015), and these effects bring together electrohydrodynamic and electrokinetic (Mukherjee, 1981). Besides, the electric charge in the liquid is loaded by the Maxwell stress, which is expressed as (Kang, 2002) $\boldsymbol{T}^{\mathrm{M}} = \varepsilon_0\varepsilon\boldsymbol{E}\otimes\boldsymbol{E} - \frac{\varepsilon_0\varepsilon}{2}(\boldsymbol{E}\cdot\boldsymbol{E})\mathbf{I}$, where ε_0 is the vacuum permittivity, ε is the liquid relative permittivity, $\boldsymbol{E}$ is the electric field vector, and $\mathbf{I}$ is the second-order unit tensor. The motion of the liquid would be affected by this load. Therefore, both the wettability and motion of the liquid can be controlled by the electric field.

Here, we present that viscous fingering in complex fluids with different relative permittivities shows a controllable performance under an electric field. Altered by an electric field, this type of viscous fingering can be actively controlled, including suppression and promotion. In this work, we define this type of viscous fingering as electro-visco-fingering (EVF). To investigate the mechanism of active control EVF, a theoretical analysis is performed to explain the phenomena observed in the experiments. The theoretical model indicates that the behavior of EVF is managed by the competition between the hydrostatic pressure and Maxwell stress. At the interface, there is a Maxwell stress jump to compete with the hydrostatic pressure gradient under an electric field. When the Maxwell stress jump assists or counteracts the hydrostatic pressure gradient, viscous fingering is enhanced or suppressed under electric fields. Due to the Maxwell stress jump and hydrostatic pressure gradient being related to the applied voltage and the flow rate, the control effect can be controlled by the practical design. Theoretically, an Electric Control number (E_C) is adopted to characterize the electric effect on the EVF. Using this parameter, the change rate of critical instability radius of EVF induced by an electric field can be evaluated. In addition, an energy balance analysis is performed to evaluate the energy conversion efficiency of this method. Surprisingly, there is almost no electrothermal dissipation in the EVF process.

RESULTS

Characterization of electro-visco-fingering

In this work, we designed experiments to investigate the active control of EVF under an electric field. A radial Hele-Shaw cell was constructed by two ITO glass disks separated by four stainless steel spacers with the same thickness. Two copper sheets were installed on the outer edge of the cell and connected to the power supply (Figure 1A). When an electric field is applied, the Hele-Shaw cell was a standard capacitor (Xiang, 2006). Liquids 1 and 2 were the displacing and displaced fluids, respectively. Pumped by a micro-pump, liquid 1 invades liquid 2 with a flow rate. In our experiment, the invading phase (μ_1) always had a much smaller viscosity than the defending fluid (μ_2), which invariably led to an unstable interface during displacement. The patterns of the unstable interface were captured by a CCD camera from above and

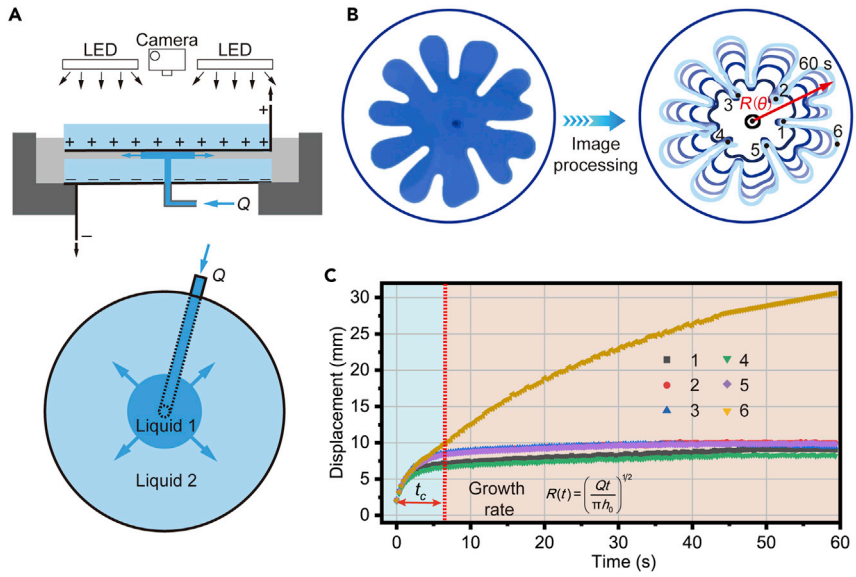

Figure 1. Experimental setup and data processing

(A) Experimental apparatus setup. Top: Side view. Bottom: Top view. Two copper sheets are installed on the outer edge of the cell, and the connected surface is the conductive side of the ITO glass. When joined with a power supply, this cell forms a uniform electric field. Flow is always injected from the center of the cell with a velocity, which is controlled by a micro-pump. Liquids 1 and 2 are the invading and defending phases, respectively.

(B) Image processing. The experimental pattern is digitized into a polar plot, and its interfacial evolution is calculated. Points 1, 2, 3, 4, and 5 are finger roots, and point 6 is a representative fingertip. In this case, the displacing and defending phases are water and silicon oil, respectively.

(C) Data processing. The displacements of points 1, 2, 3, 4, 5, and 6 over time are calculated in Python or ImageJ. t_c is the critical time when the velocity of the finger roots is zero, and the displacement of the fingertip can be written as $R(t) = [Qt/(\pi h_0)]^{1/2}$.

analyzed in Python or ImageJ (Figure 1B). As shown in Figure 1C, the interfacial evolution revealed that the fingertips are moving forward with a larger velocity, whereas the finger roots are moving slowly and even remain fixed after a time. We defined this time as the critical time (t_c), which was always less than 20 s in this work. In addition, the distance between the finger roots and the center position (injection hole) remains the same after the critical time (t_c), which is defined as the critical instability radius (r_c) in this work. According to the previous study (Beeson-Jones and Woods, 2019), when the initial and boundary conditions remain unchanged, this radius (r_c) keeps constant. Therefore, we can judge the suppression/promotion of EVF by analysing this distance and its evolutional details.

In the experiment, we used two groups of fluids to investigate the active control of EVF. In group 1, water displaced silicon oil, and the invading fluid had a larger relative permittivity than the defending fluid, which were 80.2 and 2.8. In this group, the external electric field presents a promotion effect, helping the EVF to be unstable (Figures 2A and 2B). The evolutional patterns at different voltages are shown in Figure 2A. Their forms of instability are the same, but the critical instability radius decreases when subjected to the electric field. The calculations of the average critical instability radius at different voltages are presented in Figure 2B, which are 11.8, 10.1, and 7.5 mm at 0 V, 1,000 V, and 2,000 V, respectively. Hence, the critical instability radius obviously decreases when the electric field is applied and the electric field shows a promotion effect on the EVF. In addition, the results also show that the critical instability radius is related to the applied voltage. The critical instability radius decreases with increasing applied voltages (Figure 2B). In this group, the interface of EVF is destabilized faster at higher voltages and the evolutional details are shown in Figure S1. And the same phenomena were also found in different types of fluids, such as deionized water/silicon oil, 2.0 wt % sodium chloride solution/silicon oil, and 2.0 wt % calcium chloride solution/silicon oil (Figure S2). In group 2, glycerine is invaded by silicon oil, and glycerine has a larger relative permittivity than silicon oil, which were 56.2 and 2.8. In this group, the opposite trend was found under the electric field. The evolutional patterns of interfacial instability show that the average critical instability radius increases under the electric field (Figure 2C). The radii are 8.4, 9.9, and 14.3 mm at 0 V, 1,000 V, and 2,000 V, respectively (Figure 2D). The EVF is suppressed by the applied electric field in this group and its evolutional details

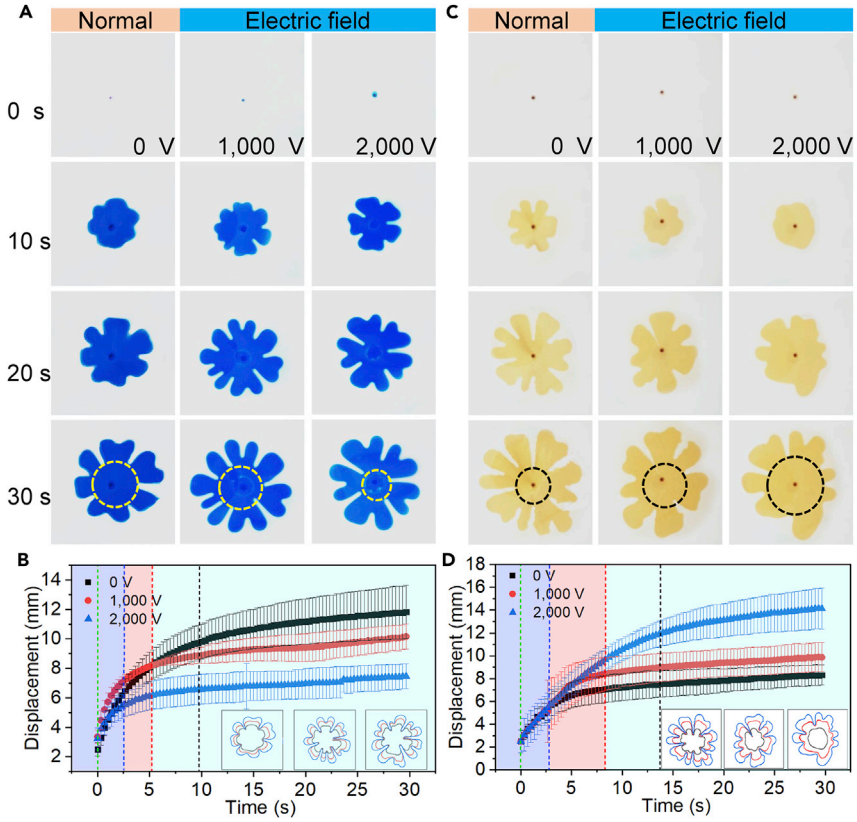

Figure 2. Examples of EVF promotion and suppression under an electric field (1 mL/min)

(A) Promotion of EVF. Silicon oil is displaced by a water phase ($\mu_2/\mu_1 = 5,000$). The silicon oil is light gray, and the water is dyed blue. A yellow dotted line is used to mark the critical instability circle.

(B) Evolution of nondominant points at different voltages. The orange dotted line is used to mark the initial moment, and the blue, red, and black dotted lines are used to mark the critical time at 0 V, 1,000 V, and 2,000 V, respectively. The evolutional details of the critical instability radius of EVF at different voltages are presented in Figure S1.

(C) Suppression of EVF. Glycerine with light gray and silicon oil with red are displaced and displacing phases, respectively ($\mu_2/\mu_1 = 300$). A black dotted line marks the critical instability circle.

(D) Evolution of nondominant points at different voltages. Its evolutional details are shown in Figure S1. The error bars in B and D are the standard deviation of the experimental data.

are presented in Figure S1. Hence, the promotion and suppression of EVF are achieved in the experiment, and the critical instability radius shows a clear relation with the applied voltage. Adjusted by an applied voltage, active control of EVF is perhaps achieved.

The theoretical model building

To clearly understand the transition in the interfacial behavior observed in the experiments and further explain the variety of critical instability radii of EVF under the electric field, we analyze the onset of the instability in the presence of an electric field. In this work, a radial Hele-Shaw cell is used with depth h_0 and radius r (Figure 3A). Fluid 2 with density ρ_2 and viscosity μ_2 is displaced by fluid 1 with density ρ_1 and viscosity μ_1. Here, the fluids can be considered incompressible due to the system having a small velocity. Because the working characteristic length (10^{-4} m) in this work is much smaller than that of the Bond number (10^{-3} m) (Zhao, 2012), the effect of fluid gravity can be neglected. As $h_0 \ll r$, the governing equations of the system are the depth-averaged Darcy's law and the mass conservation equation, which can be expressed as

$$\boldsymbol{v} = -\frac{h^2}{12\mu}\nabla p \quad \text{and} \quad \nabla\cdot\boldsymbol{v} = 0, \qquad \text{(Equation 1)}$$

where p and $\boldsymbol{v}$ are the depth-averaged pressure and velocity, respectively. This governing equation (Equation 1) is suitable for analyzing the invading and defending phases because they stay in

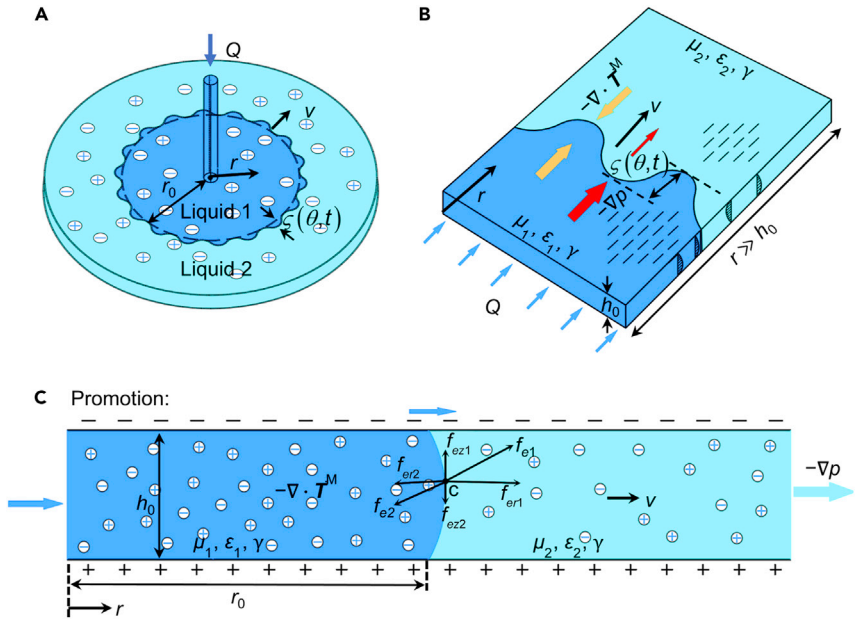

Figure 3. Mechanisms of active control of EVF in a Hele-Shaw cell

(A and B) A schematic illustrating the top view of fluid displacement in a radial Hele-Shaw cell. The uniform interface between the two fluids is perturbed in the azimuthal direction $\varsigma(\theta,t)$. The interface is always unstable when displacing fluid has a smaller viscosity than defending phase. Liquids 1 and 2 are displacing and displaced phases, respectively. Under an electric field, a Maxwell stress (T^M) is existed in the EVF. μ_1 and ε_1 are the viscosity and relative permittivity of the displacing phase, respectively, and μ_2 and ε_2 are the viscosity and relative permittivity of the displaced phase.

(C) A side view illustrating the Maxwell stress jump at the interface. According to the Korteweg-Helmholtz law (Zhao, 2012, 2014; Podosenov et al., 2012), the horizontal and vertical component of Maxwell force at the interface are $\varepsilon_0\varepsilon_j U^2/(2h_0)$ and $\varepsilon_0\varepsilon_j U^2 \cot\theta/(2h_0)$, respectively (Data S1). Owing to the interface contained in fluids with different relative permittivities, there is a Maxwell stress jump of $\varepsilon_0(\varepsilon_1-\varepsilon_2)U^2/(2h_0{}^2)$ at the interface.

the same conditions. As the experiments are conducted under an electric field, the EVF behavior is managed by coupling with the hydrostatic pressure gradient and the Maxwell stress jump $\Delta T_{er} = \varepsilon_0(\varepsilon_1 - \varepsilon_2)U^2/(2d^2)$, where U is the applied voltage, d is the distance to the surface of the dielectric layer, ε_1 and ε_2 are the relative permittivity of displacing and displaced phases, respectively (Data S1). Altered by the electric field, the Maxwell stress can be precisely controlled. Consider that the interface propagates radially with velocity $v(t)$ and is perturbed by a small-amplitude mode in the azimuthal direction $\varsigma(\theta,t) = \varsigma_0 r_0 e^{in\theta+\sigma t}$, where ς_0 is a small dimensionless parameter, r_0 is the radius of the interface, σ and n are the growth rate and dimensionless wavenumber, respectively. The kinematic boundary condition ensures that both fluids move with the same velocity at the interface. In addition, the Young-Laplace equation describes the pressure drop at the interface due to the surface tension γ. In the presence of a Maxwell stress jump, the dispersion relation is

$$(1+\lambda)\frac{\sigma r_0}{v} = -(1+\lambda)+\left[1-\lambda+\frac{\varepsilon_0(\varepsilon_1-\varepsilon_2)U^2/(2h_0\gamma)+h_0^2/r_0^2}{\mathrm{Ca}}\right]n-\frac{h_0^2/r_0^2}{\mathrm{Ca}}n^3. \qquad \text{(Equation 2)}$$

Here, $\lambda = \mu_1/\mu_2$ represents the contrast in the viscosity of fluids, and $\mathrm{Ca} = 12\mu_2 v/\gamma$ is a characteristic capillary number. In contrast to the normal system, the dispersion relation in Equation 2 includes an offset term $\varepsilon_0(\varepsilon_1 - \varepsilon_2)U^2/(2h_0\gamma\mathrm{Ca})$, which affects the stability of the interface during the displacement process (Homsy, 1987; Paterson, 1981). In the absence of an electric field or a difference in the relative permittivity of fluids, the dispersion relation in Equation 2 reduces to a well-known result (Dias and Miranda, 2010; Dias et al., 2010; Fontana et al., 2014). This dispersion relation contains three independent small parameters $\varepsilon_0(\varepsilon_1 - \varepsilon_2)U^2/(2\gamma h_0)$, h_0/r_0 and Ca, allowing for several different scenarios within the electrical parameters. This also indicates that the contribution of the Maxwell stress jump offers an opportunity to control EVF. Combined with these parameters, the critical number of fingers is set, which is expressed as

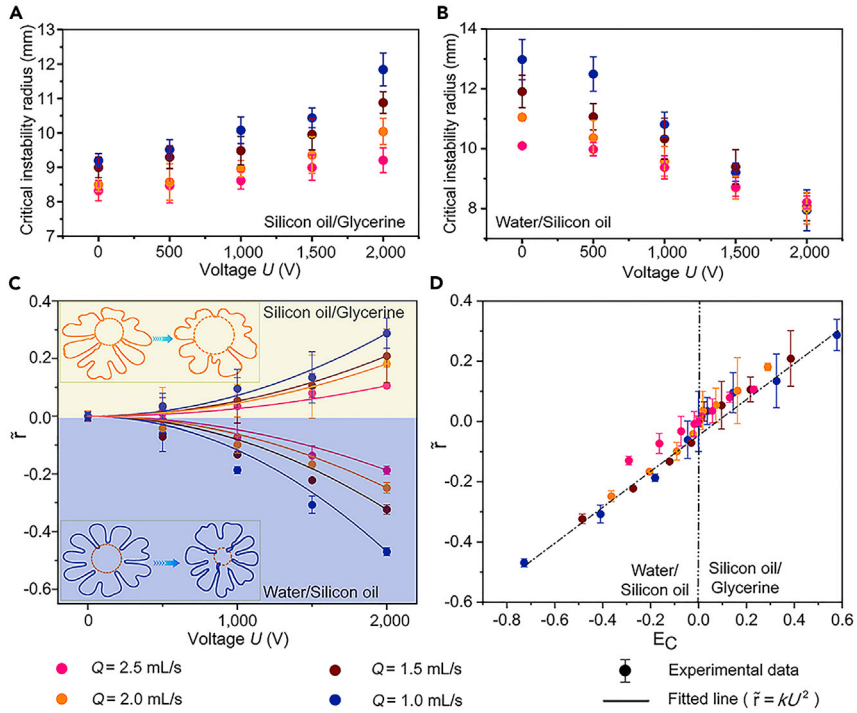

Figure 4. Controllability diagram at different flow rates and voltages

(A) Relationship between the critical instability radius and voltage (silicon oil/glycerine). A clear trend can be seen that the critical instability radius increases with increasing voltage. The critical instability radius decreases with increasing flow rate. At a high flow rate, the critical instability radius is very small, showing an unobvious change with voltage.

(B) Relationship between the critical instability radius and voltage (water/silicon oil). In this situation, the critical instability radius decreases with increasing voltage.

(C) Relationship between the critical instability radius change rate and voltage. The solid lines represent the fitted line ($\tilde{r} = kU^2$) at different flow rates, and discrete points are the experimental results.

(D) Dimensionless controllability diagram. The relationship between $\tilde{r}$ and E_C. The positive and the negative of E_C represent the experiments performed in the silicon oil/glycerine and water/silicon oil group, respectively. The error bars in A-D are the standard deviation of the experimental data.

$$n_c = \frac{1}{\sqrt{3}} \frac{Ca^{1/2}}{h_0/r_0}\left[1 - \lambda + \frac{\varepsilon_0(\varepsilon_1 - \varepsilon_2)U^2/(2h_0\gamma) + h_0^2/r_0^2}{Ca}\right]^{1/2}. \quad \text{(Equation 3)}$$

We infer from Equations 2 and 3 that the Maxwell stress jump contributes a controlling effect on the EVF. At the interface, the Maxwell stress jump is written as $\varepsilon_0(\varepsilon_1 - \varepsilon_2)U^2/(2h_0^2)$. A positive Maxwell stress jump contributes a positive offset term and has a destabilizing effect on the EVF. In contrast, a negative Maxwell stress jump has a stabilizing effect on the EVF. In our experiment, the relative permittivity of the water phase, silicon oil, and glycerine are 80.2, 2.8, and 56.2, respectively. A positive Maxwell stress jump and a negative Maxwell stress jump are presented in water/silicon oil and silicon/glycerine group, respectively. Hence, the EVF would be promoted and suppressed to be unstable in the water/silicon oil and silicon oil/glycerine group, respectively. This result is consistent with the experimental results presented in Figure 2.

Critical instability radius analysis

To examine the validity of the controllable conditions, systematic experiments were performed at different flow rates and voltages. The experimental observations presented that the promotion or suppression of viscous fingering is more obvious at higher voltages (Figures 4A and 4B). With increasing applied voltage, the critical instability radius decreases in the water/silicon oil group but increases in the silicon oil/glycerine group. The change trends of the critical instability radius are the same at different flow rates. To characterize the electric effect on the EVF, the change rate of critical instability radius induced by the electric field is written as

$$\tilde{r} = \frac{r_e - r_n}{r_n}, \quad \text{(Equation 4)}$$

where r_e and r_n represent the critical instability radius of EVF under the electric field and in the normal state, respectively. The previous studies (Orr and Taber, 1984; Draga et al., 2018) have proved that, at a small velocity, the length of fingers is almost linear with the flow rate. Because the length of fingers in these works is always characterized by an identical outer circular radius and an inner circular radius, the inner circular radius also shows a linear correlation with flow rate. In our experiment, the flow rate is small enough to meet the reporting requirements of flow rate (Pihler-Puzovic et al., 2012; Draga et al., 2018), and the inner circular radius is defined as the critical instability radius. Then, characterized by the change rate of capillary number under an electric field, the behavior of critical instability radius can be evaluated. The above analysis has proved that the motion of EVF is managed by the competition between the Maxwell stress jump and the hydrostatic pressure gradient. The parameter explored to reveal the electric effect in Equation 2 is expressed as

$$E_C = -\frac{\varepsilon_0(\varepsilon_1 - \varepsilon_2)U^2}{2h_0\gamma Ca} = -\frac{\varepsilon_0(\varepsilon_1 - \varepsilon_2)U^2}{24\mu_2 v h_0}. \quad \text{(Equation 5)}$$

This number is defined as the Electric Control number in this work. Under an electric field, the capillary number of EVF is expressed as $Ca_e = -\frac{h_0^2}{\gamma}\left[-\frac{6\mu_2 Q_n}{\pi r h_0^3} - \frac{\varepsilon_0(\varepsilon_1-\varepsilon_2)U^2}{2h_0{}^3}\right]$ (Data S1). By analysis, the Electric Control number also reveals the change rate of capillary number induced by the electric field. Therefore, characterizing by E_C, the change rate of critical instability radius would be evaluated. Inferring from Equation 5, the Electric Control number is related to the square of the applied voltage. The relationship between $\tilde{r}$ and U is plotted in Figure 4C. The discrete points are the change rate of the critical instability radius in experiments, and the solid line is the fitted line ($\tilde{r} = kU^2$). It is presented that the change rate of critical instability radial is in good agreement with the fitted line and has a quadratic relation with voltage (Table S1). The change rate of critical instability radius increases with increasing the applied voltage. On the other hand, the fitted parameters (k) calculated with the velocity of 1.0, 1.5, 2.0, and 2.5 mL/min are $k_{1.0}$, $k_{1.5}$, $k_{2.0}$, and $k_{2.5}$, respectively. $k_{1.0}/k_{1.5}$, $k_{1.0}/k_{2.0}$, and $k_{1.0}/k_{2.5}$ are 1.45, 1.89, and 2.51 in the water/silicon oil group, respectively, and 1.38, 1.58, and 2.72 in the silicon oil/glycerine group. Therefore, the change rate of critical instability radius is almost inversely proportional to the velocity. The extended plots of relative electric effect at different flow rates are presented in Figure S3 and the representative relation of $\tilde{r}$ and E_C versus the applied voltage is shown in Figure S2. In addition, the relationship between $\tilde{r}$ and E_C is presented in Figure 4D. The suppression and promotion of viscous fingering are related to the positive and negative of E_C. And $\tilde{r}$ is almost linearly related to E_C. Therefore, when the Maxwell stress jump assists or counteracts the pressure gradient, viscous fingering is suppressed or promoted. The error bars of the data points represent the uncertainties in the critical instability radius. Within the uncertainties, an excellent agreement is shown between the predicted and experimental data.

DISCUSSION

Above, we have provided experimental evidence for active control of EVF via an electric field. The experimental observations presented that the interface in complex fluids with different relative permittivities has a controllable performance under the electric field. Altered by an electric field, the EVF decay could be promoted/suppressed. Based on the theoretical analysis, active control of EVF is achieved via the competition between the hydrostatic pressure gradient and Maxwell stress jump. When the Maxwell stress jump is positive/negative, it assists/counteracts the hydrostatic pressure gradient at the interface and has a destabilizing/stabilizing effect on the EVF (Figure 2). It is the first demonstration of interfacial instability can be controlled by coupling the Maxwell stress and hydrostatic pressure. The electric effect is related to the ratio of Maxwell stress jump to the hydrostatic pressure gradient. As the hydrostatic pressure gradient and Maxwell stress drop are affected by the flow rate and applied voltage, the electric effect on the EVF is easily suited to applications. In addition, the theoretical analysis reveals that the electric effect on the EVF is linear with the square of the applied voltage that EVF would show more efficient controllability at higher voltages (Data S2). Because some irregular instability fingerings are found in the displacement process, their patterns have smaller and denser fingers than those at low voltage (Figure S3). The electric efficiency may not be infinitely improved by increasing the voltage. In addition, E_C represents the electric effect on EVF and the results show that the change rate of critical instability radius ($\tilde{r}$) is almost linear with E_C. Characterized by E_C, the change of critical instability radius and the behavior of EVF would be predicted.

Although many ways have been proposed to control viscous fingering, the method in this work is quite different from them. It is first presented that viscous fingering with different relative permittivities in displacing and displaced fluids shows a controllable performance under the electric field. Due to the relative permittivity being different in distinct materials, this method would possibly be used in the extension. Beyond the canonical case of immiscible fluids, it would be applicable to miscible liquids when the given fluids have different electrical parameters. In previous studies (De Wit, 2016; Homsy, 1987; Parisi, 1992), porous media were the most expansive practical systems for viscous fingering, which showed extremely complicated application conditions, including the heterogeneity and anisotropy of the pore space, and discontinuous liquid distribution. This always limits the implementation of many methods in applications. Due to the similarity of the governing equations in our method to those in porous media, the finding of active control of EVF in the Hele-Shaw cell may also be applicable to porous media. In particular, many statuses (Bera and Babadagli, 2015; Bogdanov et al., 2011) of electro-heating have been used for enhanced oil recovery in practical applications. By applying similar electric fields to applications of water displacing oil, it can suppress the oil/water fingering, thus making enhanced oil recovery possible by EVF. The capillary number in this work typically ranges from 10^{-3} to 10^{-2}; due to it being below the critical value for a wetting transition, the possibility of wetting films in our analysis could be ignored.

Electro-osmotic flow, which has been proven in previous studies (Gao et al., 2019; Mirzadeh and Bazant, 2017), is a well-known method for active control of viscous fingering under electric fields. In the electro-osmotic flow, viscous fingering instability can be either enhanced or suppressed by the magnitude and direction of the electric current. In this article, the method presented for active control of EVF under the electric field is fundamentally different from the electro-osmotic flow. Firstly, the active control of EVF is achieved by altering the Maxwell stress jump at the interface and the electro-osmotic flow has a weaker effect. As shown in Figure 1A, the Hele-Shaw cell is a standard capacitor and there is no current through the fluid field when a DC external electric field is applied. As there are different permittivities and conductivities in two fluids, a distinct surface potential would appear at the plates. In addition, due to the interface being a curved meniscus, there would be an electro-osmotic flow near the interface to affect the local pressure, which can be described by Helmholtz-Smoluchowski (HS) equation (Bazant and Squires, 2004, 2010) $v_{eo} = -\varepsilon_0\varepsilon_j\zeta_j E/\mu_j$, where ζ_j is the surface potential of phase j. Combined with interfacial features (Figure S4), this velocity can be expressed as $v_{eo} = -\varepsilon_0\varepsilon_j\zeta_j E\sin(2\theta_c)/(2\mu_j)$, which is along the radial direction. Take group 1 as an example, due to the polar of the water phase being considerably larger than the oil, the effect of the electric field on viscous fingering is dominated by ε_1 and ζ_1, but is almost independent on ε_2 and ζ_2. The experimental results reported (Kosmulski and Matijevic, 1992; Romero et al., 2018) for the surface potential of KCl solution with the same concentration and pH is about -20 mV. Considering the induced-charge electro-osmosis (ICEO) phenomena (Squires and Bazant, 2004; Bazant and Squires, 2010), the total zeta potential is also much less than the 188 mV. The velocity of electro-osmotic flow is compared with the hydraulic velocity induced by the Maxwell stress with the scaling of $12\zeta_j\sin(2\theta_c)/U$. Substituting these experimental data into the theoretical analysis, it can be obtained that the effect of electro-osmotic flow is much smaller than the effect brought by the Maxwell stress and the contribution of the former is less than 0.9%. Therefore, the electro-osmotic flow has a weaker effect on the EVF and can be ignored. Secondly, due to the electro-osmotic flow being related to the practical current, it needs to be applied in liquids with high conductivity. Hence, the EVF would have broader applications. Finally, to characterize the energy conversion efficiency of the two methods, an energy balance analysis is established in Data S3. The effective power in the EVF and electro-osmotic flow are $\varepsilon_0(\varepsilon_1-\varepsilon_2)U_M{}^2Q/(2h_0{}^2)$ and $\varepsilon_0(\varepsilon_w-\varepsilon_o)(v_n+v_{eo})U_{eo}{}^2s_{eo}/(2l^2)$, respectively. The magnitudes of the effective power in the two methods are of the same order. As the resistance of electrolyte solution is too large, the dissipation energy in the electro-osmotic flow is very severe (Figure S4). Its energy conversion efficiency is only 4.1%, and most electric energy is converted into heat dissipation. In the EVF, the electrical losses can be almost ignored, which shows a considerable achievement in energy-saving.

Conclusions

In this work, we report that EVF shows a controllable performance under an electric field when the relative permittivity is different in the displacing and displaced fluids. Adjusted by the electric field, active control of the interfacial instability is achieved, including suppression and promotion. To clearly explain the experimental observations, a theoretical model is established from the perspective of force analysis. Theoretically, it is indicated that a Maxwell stress jump at the interface competes with a hydrostatic pressure

gradient to achieve the active control of EVF. When the Maxwell stress jump assists/counteracts the hydrostatic pressure gradient, EVF is achieved to control under the electric field. Tuning the strength of the electric field, the electric effect on the EVF also can be controlled, which is characterized by an Electric Control number (E_C) in the model. Using this dimensionless number, the variation of the critical instability radius can be evaluated in the experiment. From the energy balance analysis, this new method presented in this article also shows a considerable achievement in energy conversion. Furthermore, active control of EVF via Maxwell stress jump under the electric field may find diverse applications and attract broad interest from various academic and industrial communities. Electric field suppression of the interfacial instability would increase the efficiency of enhanced oil recovery, whereas electric field promotion could enhance the mixing efficiency in microfluidics and porous media, such as in CO_2 sequestration. More generally, this work exemplifies the rich physics of "active manipulation of electro-visco-fingering," which might lead to new applications in confined geometries.

Limitations of the study

In this work, the theoretical model is based on a two-dimensional interfacial model in which displacement is calculated by a depth-averaged law, and some three-dimensional effects and dynamic wetting effects are not considered. Hence, some three-dimensional effects should be considered in the future when they significantly impact the flow motion.

STAR★METHODS

Detailed methods are provided in the online version of this paper and include the following:

- KEY RESOURCES TABLE
- RESOURCE AVAILABILITY
  - Lead contact
  - Materials availability
  - Data and code availability
- EXPERIMENTAL MODEL AND SUBJECT DETAILS
- METHOD DETAILS
  - Fabrication of Hele-Shaw cells
  - Preparation of electrolyte solution
  - Characterization of the displacement of electro-visco-fingering
- QUANTIFICATION AND STATISTICAL ANALYSIS
- ADDITIONAL RESOURCES

SUPPLEMENTAL INFORMATION

Supplemental information can be found online at https://doi.org/10.1016/j.isci.2022.105204.

ACKNOWLEDGMENTS

This work was jointly supported by the National Natural Science Foundation of China (NSFC, Grant No. 12032019, 11872363, 51861145314), the Chinese Academy of Sciences (CAS) Key Research Program of Frontier Sciences (Grant No. QYZDJ-SSW-JSC019).

AUTHOR CONTRIBUTIONS

Y.-P.Z. conceptualized the idea and supervised the research. P. L. and X. H. conceived the idea and designed the experiment. And P. L. collected the datasets and drafted the article. All authors read, contributed to the discussion, and approved the final article.

DECLARATION OF INTERESTS

The authors declare no competing interests.

Received: June 17, 2022
Revised: August 29, 2022
Accepted: September 20, 2022
Published: October 21, 2022

REFERENCES

Al-Housseiny, T.T., and Stone, H.A. (2013). Controlling viscous fingering in tapered Hele-Shaw cells. Phys. Fluids *25*, 092102. https://doi.org/10.1063/1.4819317.

Al-Housseiny, T.T., Christov, I.C., and Stone, H.A. (2013). Two-phase fluid displacement and interfacial instabilities under elastic membranes. Phys. Rev. Lett. *111*, 034502. https://doi.org/10.1103/PhysRevLett.111.034502.

Alqatari, S., Videbæk, T.E., Nagel, S.R., Hosoi, A.E., and Bischofberger, I. (2020). Confinement-induced stabilization of the Rayleigh-Taylor instability and transition to the unconfined limit. Sci. Adv. *6*, abd6605. https://doi.org/10.1126/sciadv.abd6605.

Anjos, P.H.A., Dias, E.O., and Miranda, J.A. (2018). Fingering instability transition in radially tapered Hele-Shaw cells: Insights at the onset of nonlinear effects. Phys. Rev. Fluids *3*, 124004. https://doi.org/10.1103/PhysRevFluids.3.124004.

Anjos, P.H.A., Zhao, M., Lowengrub, J., Bao, W., and Li, S. (2021). Controlling fingering instabilities in Hele-Shaw flows in the presence of wetting film effects. Phys. Rev. E *103*, 063105. https://doi.org/10.1103/PhysRevE.103.063105.

Anjos, P.H.A., Zhao, M., Lowengrub, J., and Li, S. (2022). Electrically controlled self-similar evolution of viscous fingering patterns. Phys. Rev. Fluids *7*, 053903. https://doi.org/10.1103/PhysRevFluids.7.053903.

Arun, R., Dawson, S.T.M., Schmid, P.J., Laskari, A., and McKeon, B.J. (2020). Control of instability by injection rate oscillations in a radial Hele-Shaw cell. Phys. Rev. Fluids *5*, 123902. https://doi.org/10.1103/PhysRevFluids.5.123902.

Bazant, M.Z., and Squires, T.M. (2004). Induced-charge electrokinetic phenomena: theory and microfluidic applications. Phys. Rev. Lett. *92*, 066101. https://doi.org/10.1103/PhysRevLett.92.066101.

Bazant, M.Z., and Squires, T.M. (2010). Induced-charge electrokinetic phenomena. Curr. Opin. Colloid Interface Sci. *15*, 203–213. https://doi.org/10.1016/j.cocis.2010.01.003.

Bazant, M.Z. (2015). Electrokinetics meets electrohydrodynamics. J. Fluid Mech. *782*, 1–4. https://doi.org/10.1017/jfm.2015.416.

Beeson-Jones, T.H., and Woods, A.W. (2019). Evidence for a universal saturation profile for radial viscous fingers. Sci. Rep. *9*, 7780. https://doi.org/10.1038/s41598-019-43728-z.

Benjacob, E., Godbey, R., Goldenfeld, N., Levine, H., Mueller, T., and Sander, L.M. (1985). Experimental demonstration of the role of anisotropy in interfacial pattern-formation. Phys. Rev. Lett. *55*, 1315–1318. https://doi.org/10.1103/PhysRevLett.55.1315.

Bera, A., and Babadagli, T. (2015). Status of electromagnetic heating for enhanced heavy oil/bitumen recovery and future prospects: a review. Appl. Energy *151*, 206–226. https://doi.org/10.1016/j.apenergy.2015.04.031.

Bischofberger, I., Ramachandran, R., and Nagel, S.R. (2014). Fingering versus stability in the limit of zero interfacial tension. Nat. Commun. *5*, 5265. https://doi.org/10.1038/ncomms6265.

Bogdanov, I.I., Torres, J.A., Akhlaghi, H.A., and Kamp, A.M. (2011). The influence of salt concentration in injected water on low-frequency electrical-heating-assisted bitumen recovery. SPE J. *16*, 548–558. https://doi.org/10.2118/129909-PA.

Bongrand, G., and Tsai, P.A. (2018). Manipulation of viscous fingering in a radially tapered cell geometry. Phys. Rev. E *97*, 061101. https://doi.org/10.1103/PhysRevE.97.061101.

Brady, R.M., and Ball, R.C. (1984). Fractal growth of copper electrodeposits. Nature *309*, 225–229. https://doi.org/10.1038/309225a0.

Chen, J.M., Legendre, L., and Benner, R. (2018). A recent project shows that the microbial carbon pump is a primary mechanism driving ocean carbon uptake. Natl. Sci. Rev. *5*, 458. https://doi.org/10.1093/nsr/nwy006.

Chuoke, R.L., Vanmeurs, P., and Vanderpoel, C. (1959). The instability of slow, immiscible, viscous liquid-liquid displacements in permeable media. Trans. AIME *216*, 188–194. https://doi.org/10.2118/1141-G.

Coutinho, Í.M., and Miranda, J.A. (2020). Control of viscous fingering through variable injection rates and time-dependent viscosity fluids: beyond the linear regime. Phys. Rev. E *102*, 063102. https://doi.org/10.1103/PhysRevE.102.063102.

De Wit, A. (2016). Chemo-hydrodynamic patterns in porous media. Philos. Trans. A Math. Phys. Eng. Sci. *374*, 20150419. https://doi.org/10.1098/rsta.2015.0419.

Dias, E.O., and Miranda, J.A. (2010). Control of radial fingering patterns: a weakly nonlinear approach. Phys. Rev. E Stat. Nonlin. Soft Matter Phys. *81*, 016312. https://doi.org/10.1103/PhysRevE.81.016312.

Dias, E.O., Parisio, F., and Miranda, J.A. (2010). Suppression of viscous fluid fingering: a piecewise-constant injection process. Phys. Rev. E Stat. Nonlin. Soft Matter Phys. *82*, 067301. https://doi.org/10.1103/PhysRevE.82.067301.

Dias, E.O., Alvarez-Lacalle, E., Carvalho, M.S., and Miranda, J.A. (2012). Minimization of viscous fluid fingering: a variational scheme for optimal flow rates. Phys. Rev. Lett. *109*, 144502. https://doi.org/10.1103/PhysRevLett.109.144502.

Dias, E.O., and Miranda, J.A. (2013a). Taper-induced control of viscous fingering in variable-gap Hele-Shaw flows. Phys. Rev. E Stat. Nonlin. Soft Matter Phys. *87*, 053015. https://doi.org/10.1103/PhysRevE.87.053015.

Dias, E.O., and Miranda, J.A. (2013b). Control of centrifugally driven fingering in a tapered Hele-Shaw cell. Phys. Rev. E Stat. Nonlin. Soft Matter Phys. *87*, 053014. https://doi.org/10.1103/PhysRevE.87.053014.

Pihler-Puzović, D., Peng, G.G., Lister, J.R., Heil, M., and Juel, A. (2018). Viscous fingering in a radial elastic-walled Hele-Shaw cell. J. Fluid Mech. *849*, 163–191. https://doi.org/10.1017/jfm.2018.404.

Eslami, A., and Taghavi, S.M. (2017). Viscous fingering regimes in elasto-visco-plastic fluids. J. Nonnewton. Fluid Mech. *243*, 79–94. https://doi.org/10.1016/j.jnnfm.2017.03.007.

Farajzadeh, R., Eftekhari, A.A., Dafnomilis, G., Lake, L.W., and Bruining, J. (2020). On the sustainability of CO_2 storage through CO_2-enhanced oil recovery. Appl. Energy *261*, 114467. https://doi.org/10.1016/j.apenergy.2019.114467.

Feng, J.T., Wang, F.C., and Zhao, Y.P. (2009). Electrowetting on a lotus leaf. Biomicrofluidics *3*, 022406. https://doi.org/10.1063/1.3124822.

Fontana, J.V., Dias, E.O., and Miranda, J.A. (2014). Controlling and minimizing fingering instabilities in non-Newtonian fluids. Phys. Rev. E Stat. Nonlin. Soft Matter Phys. *89*, 013016. https://doi.org/10.1103/PhysRevE.89.013016.

Gao, T., Mirzadeh, M., Bai, P., Conforti, K.M., and Bazant, M.Z. (2019). Active control of viscous fingering using electric fields. Nat. Commun. *10*, 4002. https://doi.org/10.1038/s41467-019-11939-7.

Gorell, S.B., and Homsy, G.M. (1983). A theory of the optimal policy of oil-recovery by secondary displacement processes. SIAM J. Appl. Math. *43*, 79–98. https://doi.org/10.1137/0143007.

Gilmore, K.A., Neufeld, J.A., and Bickle, M.J. (2020). CO_2 dissolution trapping rates in heterogeneous porous media. Geophys. Res. Lett. *47*. e2020GL087001. https://doi.org/10.1029/2020GL087001.

Hill, S. (1952). Channelling in packed columns. Chem. Eng. Sci. *1*, 247–253. https://doi.org/10.1016/0009-2509(52)87017-4.

Homsy, G.M. (1987). Viscous fingering in porous-media. Annu. Rev. Fluid Mech. *19*, 271–311. https://doi.org/10.1146/annurev.fl.19.010187.001415.

Honda, T., Honjo, H., and Katsuragi, H. (2006). Exprimental study on the morphology in a large Hele-Shaw cell. J. Phys. Soc. Japan *75*, 034005. https://doi.org/10.1143/JPSJ.75.034005.

Holtzman, R., and Segre, E. (2015). Wettability stabilizes fluid invasion into porous media via nonlocal, cooperative pore filling. Phys. Rev. Lett. *115*, 164501. https://doi.org/10.1103/PhysRevLett.115.164501.

Islam, T.U., and Gandhi, P.S. (2016). Fabrication of multscale fractal-like structures by controlling fluid interface instability. Sci. Rep. *6*, 37187. https://doi.org/10.1038/srep37187.

Jeong, J.H., Goldenfeld, N., and Dantzig, J.A. (2001). Phase field model for three-dimensional dendritic growth with fluid flow. Phys. Rev. E Stat. Nonlin. Soft Matter Phys. *64*, 041602. https://doi.org/10.1103/PhysRevE.64.041602.

Jha, B., Cueto-Felgueroso, L., and Juanes, R. (2011). Fluid mixing from viscous fingering. Phys. Rev. Lett. *106*, 194502. https://doi.org/10.1103/PhysRevLett.106.194502.

Kang, K.H. (2002). How electrostatic fields change contact angle in electrowetting. Langmuir *18*, 10318–10322. https://doi.org/10.1021/la0263615.

Kanhurkar, S.D., Patankar, V., ul Islam, T., Gandhi, P.S., and Bhattacharya, A. (2019). Stability of viscous fingering in lifted Hele Shaw cell with a hole. Phys. Rev. Fluids *4*, 094003. https://doi.org/10.1103/PhysRevFluids.4.094003.

Köllner, T., Schwarzenberger, K., Eckert, K., and Boeck, T. (2015). Solutal Marangoni convection in a Hele-Shaw geometry: impact of orientation and gap width. Eur. Phys. J. Spec. Top. *224*, 261–276. https://doi.org/10.1140/epjst/e2015-02358-2.

Kosmulski, M., and Matijevic, E. (1992). Zeta.-potentials of silica in water-alcohol mixtures. Langmuir *8*, 1060–1064. https://doi.org/10.1021/la00040a008.

Li, S., Lowengrub, J.S., Fontana, J., and Palffy-Muhoray, P. (2009). Control of viscous fingering patterns in a radial Hele-Shaw cell. Phys. Rev. Lett. *102*, 174501. https://doi.org/10.1103/PhysRevLett.102.174501.

Liu, C., Sun, J., Zhuang, Y., Wei, J., Li, J., Dong, L., Yan, D., Hu, A., Zhou, X., and Wang, Z. (2018). Self-propelled droplet-based electricity generation. Nanoscale *10*, 23164–23169. https://doi.org/10.1039/C8NR08772E.

Maes, R., Rousseaux, G., Scheid, B., Mishra, M., Colinet, P., and De Wit, A. (2010). Experimental study of dispersion and miscible viscous fingering of initially circular samples in Hele-Shaw cells. Phys. Fluids *22*, 123104. https://doi.org/10.1063/1.3528039.

Marthelot, J., Strong, E.F., Reis, P.M., and Brun, P.T. (2018). Designing soft materials with interfacial instabilities in liquid films. Nat. Commun. *9*, 4477. https://doi.org/10.1038/s41467-018-06984-7.

Morrow, L.C., Moroney, T.J., and McCue, S.W. (2019). Numerical investigation of controlling interfacial instabilities in non-standard Hele-Shaw configurations. J. Fluid Mech. *877*, 1063–1097. https://doi.org/10.1017/jfm.2019.623.

Mirzadeh, M., and Bazant, M.Z. (2017). Electrokinetic control of viscous fingering. Phys. Rev. Lett. *119*, 174501. https://doi.org/10.1103/PhysRevLett.119.174501.

Mukherjee, S. (1981). Lippmann-Schwinger equation. Pramana J. Phys. *16*, 81–89. https://doi.org/10.1007/BF02847895.

Orr, F.M., and Taber, J.J. (1984). Use of carbon-dioxide in enhanced oil-recovery. Science *224*, 563–569. https://doi.org/10.1126/science.224.4649.563.

Parisi, G. (1992). On surface growth in random-media. Europhys. Lett. *17*, 673–678. https://doi.org/10.1209/0295-5075/17/8/002.

Paterson, L. (1981). Radial fingering in a Hele Shaw cell. J. Fluid Mech. *113*, 513–529. https://doi.org/10.1017/S0022112081003613.

Peng, G.G., and Lister, J.R. (2020). Viscous flow under an elastic sheet. J. Fluid Mech. *905*, A30. https://doi.org/10.1017/jfm.2020.745.

Podosenov, S.A., Foukzon, J., and Potapov, A.A. (2012). Electrodynamics of a continuous medium in a system with specified structure. Phys. Wave Phenom. *20*, 143–157. https://doi.org/10.3103/S1541308X12020094.

Pihler-Puzović, D., Illien, P., Heil, M., and Juel, A. (2012). Suppression of complex fingerlike patterns at the interface between air and a viscous fluid by elastic membranes. Phys. Rev. Lett. *108*, 074502. https://doi.org/10.1103/PhysRevLett.108.074502.

Pihler-Puzović, D., Peng, G.G., Lister, J.R., Heil, M., and Juel, A. (2018a). Viscous fingering in a radial elastic-walled Hele-Shaw cell. J. Fluid Mech. *849*, 163–191. https://doi.org/10.1017/jfm.2018.404.

Rabaud, M., Michalland, S., and Couder, Y. (1990). Dynamical regimes of directional viscous fingering: spatiotemporal chaos and wave-propagation. Phys. Rev. Lett. *64*, 184–187. https://doi.org/10.1103/PhysRevLett.64.184.

Romero, C.P., Jeldres, R.I., Quezada, G.R., Concha, F., and Toledo, P.G. (2018). Zeta potential and viscosity of colloidal silica suspensions: effect of seawater salts, pH, flocculant, and shear rate. Colloids Surf. A Physicochem. Eng. Asp. *538*, 210–218. https://doi.org/10.1016/j.colsurfa.2017.10.080.

Saffman, P.G., and Taylor, G. (1958). The penetration of a fluid into a porous medium or Hele-Shaw cell containing a more viscous liquid. Proc. R. Soc. Lond. Ser. A *245*, 312–329. https://doi.org/10.1098/rspa.1958.0085.

Schnitzer, O., Frankel, I., and Yariv, E. (2014). Electrophoresis of bubbles. J. Fluid Mech. *753*, 49–79. https://doi.org/10.1017/jfm.2014.350.

Schnitzer, O., and Yariv, E. (2015). The Taylor–Melcher leaky dielectric model as a macroscale electrokinetic description. J. Fluid Mech. *773*, 1–33. https://doi.org/10.1017/jfm.2015.242.

Squires, T.M., and Bazant, M.Z. (2004). Induced-charge electro-osmosis. J. Fluid Mech. *509*, 217–252. https://doi.org/10.1017/S0022112004009309.

Tadmor, R., Hernández-Zapata, E., Chen, N., Pincus, P., and Israelachvili, J.N. (2002). Debye length and double-layer forces in polyelectrolyte solutions. Macromolecules *35*, 2380–2388. https://doi.org/10.1021/ma011893y.

Taheri, A., Torsæter, O., Lindeberg, E., Hadia, N.J., and Wessel-Berg, D. (2018). Qualitative and quantitative experimental study of convective mixing process during storage of CO_2 in heterogeneous saline aquifers. Int. J. Greenh. Gas Control *71*, 212–226. https://doi.org/10.1016/j.ijggc.2018.02.003.

Taylor, G.I. (1963). Cavitation of a viscous fluid in narrow passages. J. Fluid Mech. *16*, 595–619. https://doi.org/10.1017/S0022112063001002.

Trojer, M., Szulczewski, M.L., and Juanes, R. (2015). Stabilizing fluid-fluid displacements in porous media through wettability alteration. Phys. Rev. Appl. *3*, 054008. https://doi.org/10.1103/PhysRevApplied.3.054008.

Vaquero-Stainer, C., Heil, M., Juel, A., and Pihler-Puzović, D. (2019). Self-similar and disordered front propagation in a radial Hele-Shaw channel with time-varying cell depth. Phys. Rev. Fluids *4*, 064002. https://doi.org/10.1103/PhysRevFluids.4.064002.

Wooding, R.A., and Morelseytoux, H.J. (1976). Multiphase fluid-flow through porous-media. Annu. Rev. Fluid Mech. *8*, 233–274. https://doi.org/10.1146/annurev.fl.08.010176.001313.

Xu, W., Wang, J., Ding, F., Chen, X., Nasybulin, E., Zhang, Y., and Zhang, J.G. (2014). Lithium metal anodes for rechargeable batteries. Energy Environ. Sci. *7*, 513–537. https://doi.org/10.1039/C3EE40795K.

Xiang, Y. (2006). The electrostatic capacitance of an inclined plate capacitor. J. Electrostat. *64*, 29–34. https://doi.org/10.1016/j.elstat.2005.05.002.

Yuan, Q., and Zhao, Y.P. (2009). Hydroelectric voltage generation based on water-filled single-walled carbon nanotubes. J. Am. Chem. Soc. *131*, 6374–6376. https://doi.org/10.1021/ja8093372.

Yuan, Q., and Zhao, Y.P. (2010). Precursor film in dynamic wetting, electrowetting, and electro-elasto-capillarity. Phys. Rev. Lett. *104*, 246101. https://doi.org/10.1103/PhysRevLett.104.246101.

Zhao, Y.P. (2012). Physical Mechanics of Surfaces and Interfaces (Science Press).

Zhao, Y.P. (2014). Nano and Mesoscopic Mechanics (Science Press).

Zheng, Z., Kim, H., and Stone, H.A. (2015). Controlling viscous fingering using time-dependent strategies. Phys. Rev. Lett. *115*, 174501. https://doi.org/10.1103/PhysRevLett.115.174501.

STAR★METHODS

KEY RESOURCES TABLE

REAGENT or RESOURCE	SOURCE	IDENTIFIER
Chemicals, peptides, and recombinant proteins		
Silicon oil	Shin-Etsu Chemical Co., Ltd.	CAS: 63148-62-9
Glycerine	Aladdin Reagent (Shanghai) Co., Ltd.	CAS: 56-81-5
NaCl (AR 99.5%)	Aladdin Reagent (Shanghai) Co., Ltd.	CAS: 7647-14-5
KCl (AR 99.5%)	Aladdin Reagent (Shanghai) Co., Ltd.	CAS: 7447-40-7
$CaCl_2$ (AR 96%)	Aladdin Reagent (Shanghai) Co., Ltd.	CAS: 10043-52-4
Deposited data		
Interfacial evolutions	This manuscript	https://doi.org/10.17632/z2fkd7y2gb.1
Custom Program code	This manuscript	https://doi.org/10.17632/p3xr562ph4.1
Software and algorithms		
Origin 2018	Origin lab corporation	https://www.originlab.com
Microsoft Visual Studio-Python	Microsoft	https://visualstudio.microsoft.com/vs/features/python/
ImageJ	National Institutes of Health	https://imagej.nih.gov/ij/

RESOURCE AVAILABILITY

Lead contact

Further information and requests for resources and reagents should be directed to and will be fulfilled by the Lead Contact, Ya-Pu Zhao (yzhao@imech.ac.cn).

Materials availability

This study did not generate new unique reagents.

Data and code availability

Interfacial evolutions reported in this paper have been deposited at Mendeley Data and are publicly available as of the date of publication. The DOI is listed in the key resources table. Interfacial evolutions are analyzed using a custom written Python code. The critical instability radius used in the figures is calculated from the mean value and standard deviations. The statistical analysis detail can be found in the figure captions and method details. All original code has been deposited at Mendeley Data and is publicly available as of the date of publication. The DOI is listed in the key resources table. Any additional information required to reanalyze the data reported in this paper is available from the lead contact upon request.

EXPERIMENTAL MODEL AND SUBJECT DETAILS

This study does not use experimental methods typical in the life sciences.

METHOD DETAILS

Fabrication of Hele-Shaw cells

In the experiment, the circular ITO glass (15 cm in diameter, 0.11 cm in thickness, and 7.0 in relative permittivity) was used with a resistance of only 6 Ω. Before each setup, the ITO glass was rinsed in an alcohol solution (99.97%) to remove the dust. After surface drying, two circular ITO glass plates were stacked together, separated by four stainless steel spacers, to construct Hele-Shaw cells. The stainless steel spacers with the thickness of 200 and 500 μm were used to construct the Hele-Shaw cell with gaps of 200 and 500 μm, respectively. And the water/silicon oil and silicon oil/glycerine group were conducted in Hele-Shaw cells with a gap of 500 and 200 μm, respectively. Such gap settings were mainly applied to obtain an instability area suitable for observation at the same displacement speed. ITO glass was conductive

on one side but nonconductive on the other side. Both copper sheets were housed on the conductive side in the experimental setup and connected with a power supply (677B, Trek, USA).

Preparation of electrolyte solution

Two groups of fluids were used to investigate the active control of electro-visco-fingering. In group 1, water phase with a viscosity of 1.0 mPa s was the displacing phase, and silicon oil (Shin-Etsu, Japan) with a viscosity of 5,000.0 mPa s was the displaced phase. In this group, the relative permittivity of water phase was adjusted by adding 2.0 wt % KCl, NaCl, or $CaCl_2$. In group 2, silicon oil (Shin-Etsu, Japan) with a viscosity of 5.0 mPa s was the displacing fluid, and pure glycerine (Aladdin, China) with a viscosity of 1,500.0 mPa s was the displaced fluid. Silicon oil was used for its immiscibility with water (practically insoluble) and glycerine (practically insoluble), and modest surface tension (0.021 N/m). To clearly display the interface of two fluids, the displacing phases were dyed with 0.1 wt% water blue and oil red, respectively. The pH of water phase (KCl), silicon oil, and glycerine were 7.0, 6.7, and 7.0, respectively.

Characterization of the displacement of electro-visco-fingering

Before each test, liquid 2 was preset in Hele-Shaw cells. After tuning on the supply power, liquid 1 would be invaded from the center of ITO glass to displace liquid 2, and its flow rates were controlled by a micropump (Pump 11 Elite, Harvard Apparatus, USA). A camera (JHUM1204s-E, Jinghang, China), mounted on an independent *XYZ* stage, was used to record this displacement process with 3 fps. The external voltage was applied with a precision of ± 1 V and the flow rates were controlled with a precision of 0.1 mL/min. In the experiment, the flow rates of 1.0, 1.5, 2.0, and 2.5 mL/min and the voltages of 500, 1,000, 1,500, and 2,000 V were used. All experiments were carried out at room temperature (20°C).

QUANTIFICATION AND STATISTICAL ANALYSIS

The raw experimental data were generated by ImageJ/Python software (Figure 1C). The Interfacial evolutions were analyzed using a custom Python code. The Python code has been deposited at Mendeley Data and its DOI is listed in the key resources table. We computed the interfacial evolutions of each experiment from the Python analysis, and used the ImageJ to compute the value of critical instability radius for each evolutional pattern after the critical time. All data plots for the figures in the main text and supplemental information were produced by Origin (2018) using the raw experimental data. The error bars included in the figures are the standard deviation of the experimental data. Information about the error bars is provided in the legends (Figures 2 and 4).

ADDITIONAL RESOURCES

Our study has not generated or contributed to a new website/forum or not been a part of a clinical trial.